


Article

Compact-Transmission-Line Decoupling and Matching Network of Three-Element Array for Wireless Applications

Chi Zhang *  and Yong-Chang Jiao

National Key Laboratory of Antennas and Microwave Technology, Xidian University, Xi'an 710071, China

* Correspondence: zhch92@gmail.com

Abstract: In this paper, a compact-transmission-line (TL) decoupling and matching network (DMN) for three-element circular arrays is presented. As a result of the miniaturization of wireless terminals, the antenna spacing is too close, leading to large couplings and deteriorating system performance. The DMN consists of an impedance transformation section and a star-shaped neutralization section which eliminates couplings between antennas while occupying a smaller area. The impedance transformation section converts the odd and even mode conductances of the antenna to the impedance of the feeding line, and the neutralization section eliminates the odd and even mode susceptances to complete the decoupling and matching of the antenna. The star-shaped circuit utilizes the area surrounded by the antennas in a more efficient manner than traditional triangle circuits. This facilitates the folding of the TL and the miniaturization of the circuit. A design formula is given for each module of the circuit after it has been analyzed analytically. A decoupling example is simulated and manufactured with the diameter of the area occupied by the DMN less than a quarter wavelength. At the working frequency, the port isolation is increased from 7.6 dB to 33.5 dB. The ECC between ports is reduced from 0.11 to 0.011, which validates the method proposed.

Keywords: mutual coupling; decoupling and matching network (DMN); multiple-input multiple-output (MIMO) antenna



Citation: Zhang, C.; Jiao, Y.-C. Compact-Transmission-Line Decoupling and Matching Network of Three-Element Array for Wireless Applications. *Electronics* **2023**, *12*, 1567. <https://doi.org/10.3390/electronics12071567>

Academic Editor: Djuradj Budimir

Received: 7 March 2023

Revised: 23 March 2023

Accepted: 25 March 2023

Published: 27 March 2023



Copyright: © 2023 by the authors. Licensee MDPI, Basel, Switzerland. This article is an open access article distributed under the terms and conditions of the Creative Commons Attribution (CC BY) license (<https://creativecommons.org/licenses/by/4.0/>).

1. Introduction

With the help of multiple-input multiple-output (MIMO) technology, the industry has proposed improving spectrum utilization efficiency without consuming more bandwidth or increasing transmit power. It is equivalent to transmitting signals from multiple antennas at one terminal and receiving signals from multiple antennas at the other end, so that the signal has a higher degree of dimension and the spectrum utilization efficiency is enhanced while maintaining the existing frequency and time diversity [1,2]. Miniaturization and portability of mobile terminals constrain the design of MIMO antennas severely. Multi-antenna systems suffer from strong mutual coupling between antennas arranged close together [3], which significantly reduces system performance. It even needs to deal with the strong coupling caused by the one-twentieth wavelength distance between the antennas [4]. There has been a growing concern about eliminating mutual coupling in research.

For multi-antenna systems, decoupling methods are generally divided into two main categories, namely, decoupling from the field and the circuit point of view. The antenna in [5] is bent and loaded with stubs at the appropriate position to adjust the beam direction. The orthogonal arrangement of antennas is also an effective method to reduce coupling between them [6–8]. It is possible to adjust the beam direction using an elevated ground [9–11] between adjacent antenna units that serves as a reflector plate. The insertion of sub-wavelength periodic structures between antennas, such as an electromagnetic band gap (EBG) [12–15], has the function of preventing interference between the antennas. The defected ground structures (DGS) [16–19] between the antennas act as a band-stop filter. An alternative coupling path can be provided by neutralization lines [20–23] or parasitic

cells [24–30], whose energy coupled has an equal magnitude and opposite phase to that coupled in space, in order to cancel the coupling. The coupling between the antennas can be effectively reduced by placing the split ring resonators [31] on the spatial coupling path [30]. An effective decoupling effect can be achieved by introducing a miniaturized ladder resonator in the gap between the antennas [29]. As a result of these methods, the radiating structures must be modified, increasing both the design complexity and time required.

The second class of decoupling methods involves cascading decoupling networks. The time consumed for the simulation of the decoupling network is much less than that of changing radiation structures. There are two types of decoupling networks: one is the eigenmode method and the other is the conjugate matching method. A disadvantage of the eigenmode method is that it is limited by the potential of the radiation structure itself, and the differential mode port's operating band is smaller than that of the common mode port. In addition, the complexity of the implemented circuit [32,33] is higher than that of the conjugate matching method. The design of the decoupling network in [34] is investigated using lumped components, which are implemented with microstrip transmission lines by Kuroda's identity. In the design principle stage of [35,36], transmission lines are used directly, which greatly reduces the circuit area. Decoupling circuits using coupled resonators are presented in [37]. For a three-element array, the current design process divides the circuit into three parts, namely, the impedance transformation circuit, the decoupling circuit, and the matching circuit, resulting in a large circuit area.

We present a circuit structure that integrates decoupling and matching at the design stage, i.e., a network for impedance transformation and a network for neutralization at the design stage. In addition, the circuit utilizes a star instead of a triangular decoupling structure, which is more effective for folding the circuit at the area surrounded by the array. Consequently, the area occupied by the matching and decoupling network is greatly reduced compared with the existing schemes [34–37]. Compared with [37], which has the best performance in miniaturization, the solution presented in this paper has a relative size reduction of 17%. A systematic presentation of the analysis method, design formulae, and design procedure of the circuit is provided in this paper.

The following is an outline of the article: The second part of the paper describes the circuits of each part of the decoupling and matching network (DMN), along with their characteristics and the closed-form formulae used to design the parameters. Presented in the third part is an example of the DMN for a three-element circular array. The fourth part of the study tests the case in order to verify the effectiveness of the method. The conclusion is given in the fifth part.

2. Decoupling Technique

2.1. Network Analysis

Figure 1 illustrates the schematic diagram of the DMN of the three-element antenna array. The network consists of series-connected impedance/admittance transformation sections (ITS) and a parallel-connected neutralization section (NS).

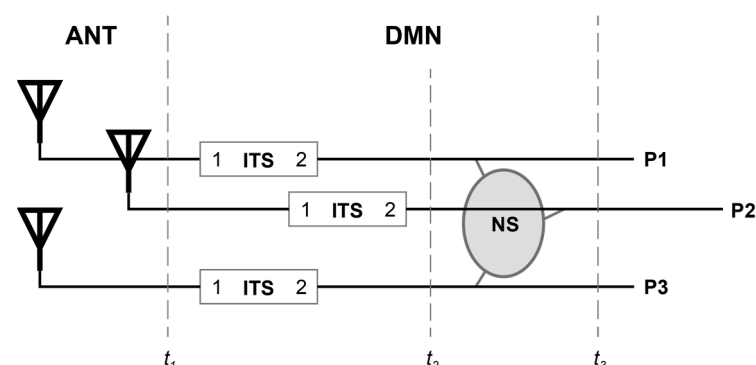


Figure 1. The DMN of a three-element circular array.

As the three-element antenna array is circularly symmetric, the admittance matrix at the reference plane t_1 is circularly symmetric as well. The main diagonal elements denoting self-admittance are equal, and the values of other elements denoting mutual-admittance are also equal as shown in the following equation

$$\mathbf{Y}^{t_1} = \begin{bmatrix} Y_{11}^{t_1} & Y_{12}^{t_1} & Y_{12}^{t_1} \\ Y_{12}^{t_1} & Y_{11}^{t_1} & Y_{12}^{t_1} \\ Y_{12}^{t_1} & Y_{12}^{t_1} & Y_{11}^{t_1} \end{bmatrix} \quad (1)$$

The decoupling and matching of the antennas are carried out at the reference plane t_3 , which means that the diagonal elements of the admittance matrix must be Y_0 , and any other elements must be 0, [34] i.e.,

$$\mathbf{Y}^{t_3} = \begin{bmatrix} Y_0 & 0 & 0 \\ 0 & Y_0 & 0 \\ 0 & 0 & Y_0 \end{bmatrix} \quad (2)$$

It is well-known that when networks are connected in parallel, the admittance matrices should be added directly. As a passive, loss-less three-port network, the neutralization section's admittance matrix consists entirely of imaginary numbers. Thus, we can reversely determine the characteristic of the admittance matrix at t_2 , that is, after the series impedance transformation section: the real part of the main diagonal element is Y_0 , and the other elements are pure imaginary numbers.

$$\mathbf{Y}^{t_2} = \begin{bmatrix} G_0 + jB_{11}^{t_2} & jB_{12}^{t_2} & jB_{12}^{t_2} \\ jB_{12}^{t_2} & G_0 + jB_{11}^{t_2} & jB_{12}^{t_2} \\ jB_{12}^{t_2} & jB_{12}^{t_2} & G_0 + jB_{11}^{t_2} \end{bmatrix} \quad (3)$$

At this point, we have analyzed the admittance matrix of each reference plane of the antenna array with a DMN. Through this direct analysis, we are able to gain a better understanding of how the two parts of the DMN work together. Nevertheless, the matrix analysis is complicated and cumbersome, which makes the subsequent quantitative design difficult. In the following paragraphs, we use the odd and even mode method to simplify the analysis.

2.2. Impedance-Transforming Section

The equivalent circuit diagram of the symmetrical three-port network is shown in Figure 2. Here, we use the odd–even mode analysis method [38] to analyze the circuit, which can greatly simplify the analysis [39]. The odd and even mode admittances of the network at the reference plane t_1 are given by [34].

$$\begin{aligned} Y_e^{t_1} &= Y_{11}^{t_1} + 2Y_{12}^{t_1} \\ Y_o^{t_1} &= Y_{11}^{t_1} - Y_{12}^{t_1} \end{aligned} \quad (4)$$

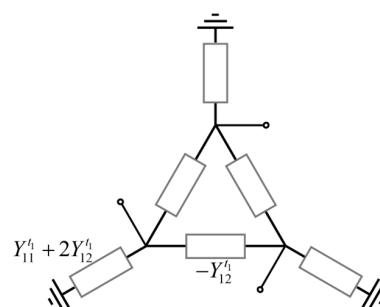


Figure 2. Equivalent circuit diagram of the symmetrical three-port network at reference plane t_1 .

According to Equation (3), the odd and even mode conductances at the reference plane t_2 should be equal to Y_0 [40].

A circuit selection for the impedance transformation module is shown in Figure 3, which consists of a parallel transmission line stub TL1 (equivalent to a conductance) and a series transmission line TL2. Therefore, at t_2 , the odd and even mode admittances are transformed into

$$Y_{e,o}^{t_2} = Y_2 \frac{(Y_{e,o}^{t_1} + jB_1) + jY_2 \tan \theta_2}{Y_2 + j(Y_{e,o}^{t_1} + jB_1) \tan \theta_2} \quad (5)$$

whose real parts are both equal to Y_0 , which can be expressed as

$$G_{e,o}^{t_2} = \frac{G_{e,o}^{t_1} (1 + \tan^2 \theta_2) Y_2^2}{G_{e,o}^{t_1} \tan^2 \theta_2 + [Y_2 - (B_1 + B_{e,o}^{t_1}) \tan \theta_2]^2} = Y_0 \quad (6)$$

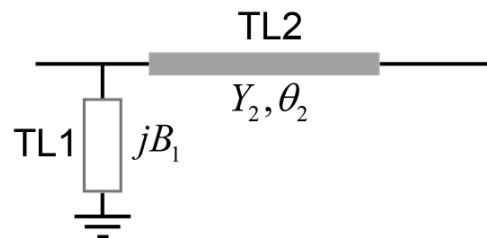


Figure 3. Diagram of the admittance transforming circuit.

By selecting the admittance of the transmission line TL2 as a known quantity, it is possible to calculate the tangent value of its electrical length as follows:

$$\tan \theta_2 = \pm Y_2 \sqrt{\frac{|Y_e^{t_1} - Y_o^{t_1}|^2 (G_e^{t_1} + G_o^{t_1}) Y_0 - (G_e^{t_1} - G_o^{t_1})^2 Y_2^2 \pm 2Y_0 |B_e^{t_1} - B_o^{t_1}| |Y_e^{t_1} - Y_o^{t_1}| \sqrt{G_e^{t_1} G_o^{t_1}}}{|Y_e^{t_1} - Y_o^{t_1}|^2 [(B_e^{t_1} - B_o^{t_1})^2 + (G_e^{t_1} + G_o^{t_1})^2] Y_0^2 - 2|Y_e^{t_1} - Y_o^{t_1}|^2 (G_e^{t_1} + G_o^{t_1}) Y_0 Y_2^2 + (G_e^{t_1} - G_o^{t_1})^2 Y_2^4}} \quad (7)$$

The electrical length corresponding to the tangent value less than zero is greater than a quarter of the wavelength, which will result in an excessively large circuit area, so we discard the two solutions. We then substitute the tangent and admittance back into formula (6). The concatenated susceptance can be obtained as follows:

$$B_1 = \frac{Y_0 (Y_2 \tan \theta_2 - B_e^{t_1} \tan^2 \theta_2) \pm \sqrt{Y_0 G_e^{t_1} \tan^2 \theta_2 [(1 + \tan^2 \theta_2) Y_2^2 - Y_0 G_e^{t_1} \tan^2 \theta_2]}}{Y_0 \tan^2 \theta_2} \quad (8)$$

In order to miniaturize the circuit, a short-circuit stub is employed when the parallel susceptance value exceeds zero, and an open-circuit stub is used when it is less than zero.

2.3. Neutralization Section

The odd and even mode conductances at the t_2 reference plane equal Y_0 . According to Equation (2), the admittances of the odd and even mode admittances at t_3 should equal Y_0 , if the decoupling and matching conditions are satisfied. In other words, the neutralization circuit has the function of eliminating the imaginary parts of the odd mode and even mode admittances.

A circuit diagram of the neutralization network is illustrated in Figure 4a, which is composed of transmission line stubs TL4 connected in parallel and transmission lines TL3 connected in a star pattern. Compared to the existing neutralization designs [26–28], this

work uses a star-shaped circuit, which occupies a smaller area when the transmission lines are folded. The even and odd admittances of the neutralization are expressed as

$$\begin{aligned} Y_e^N &= jB_4 + jY_3 \tan \theta_3 \\ Y_o^N &= jB_4 - jY_3 \cot \theta_3 \end{aligned} \quad (9)$$

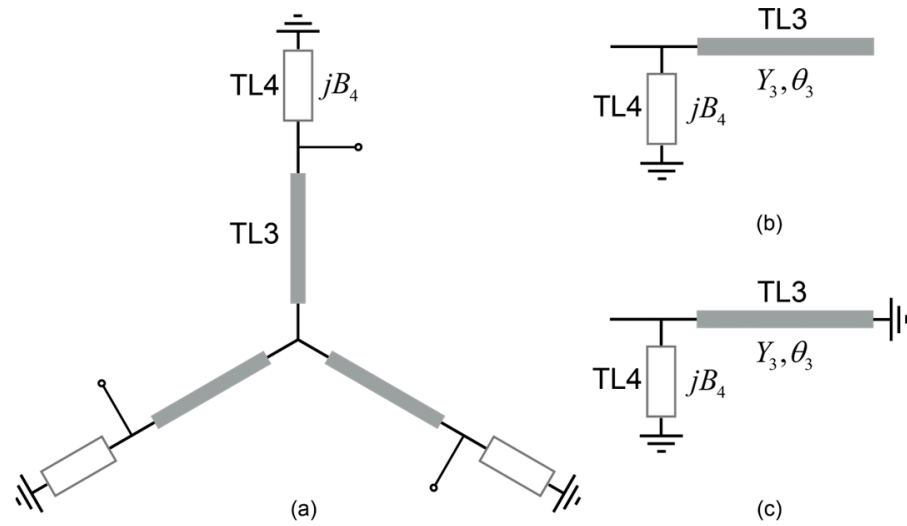


Figure 4. Equivalent circuit diagram of the neutralization section: (a) the star-shaped circuit; (b) the even mode circuit; and (c) the odd mode circuit.

To eliminate the imaginary parts of the odd mode and even mode admittances, the design parameters should be satisfied:

$$\begin{aligned} B_4 + Y_3 \tan \theta_3 &= -B_e^{t2} \\ B_4 - Y_3 \cot \theta_3 &= -B_o^{t2} \end{aligned} \quad (10)$$

The solution of the tangent is given as follows:

$$\tan \theta_3 = \frac{(B_o^{t2} - B_e^{t2}) \pm \sqrt{(B_o^{t2} - B_e^{t2})^2 - 4Y_3^2}}{2Y_3} \quad (11)$$

Substituting (11) into (10) yields

$$B_4 = -B_e^{t2} - Y_3 \tan \theta_3 \quad (12)$$

TL4 is implemented using the same methods as TL1, so this section will not repeat the procedure.

3. Design Example

3.1. Coupled Array

To evaluate the validity of the method presented in this paper, we perform a decoupling and matching operation on a coupled three-element monopole array. In Figure 5, three copper rods with a diameter of $d_a = 1.12$ mm are installed vertically at a distance of $d = 18$ mm on a circular ground with a diameter of 120 mm, forming a symmetrical three-element array. The dielectric substrate is made of F4 B material with a dielectric constant of 2.6 and a thickness of 0.8 mm.

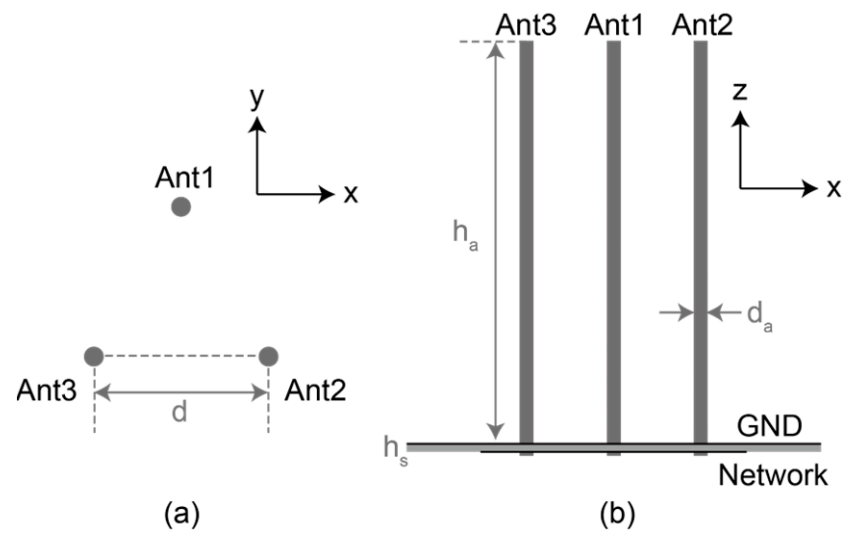


Figure 5. (a) Top view and (b) front view of the coupled three-element array.

The height of the monopole above the ground is $h_a = 28.6$ mm. The designed operating frequency is $f_0 = 2.5$ GHz, and its corresponding quarter wavelength is 30 mm. The length of h_a is smaller than it, because the strong couplings between the antennas are equivalent to the loads of the antennas resulting in the antenna-operating frequency shifting to lower frequencies. Figure 6 illustrates the simulated scattering parameters. Due to the symmetry of the three ports, only the self and mutual parameters between ports 1 and 2 are presented here. As can be seen, the antenna operates at 2.5 GHz, and the port isolation is only 7.5 dB.

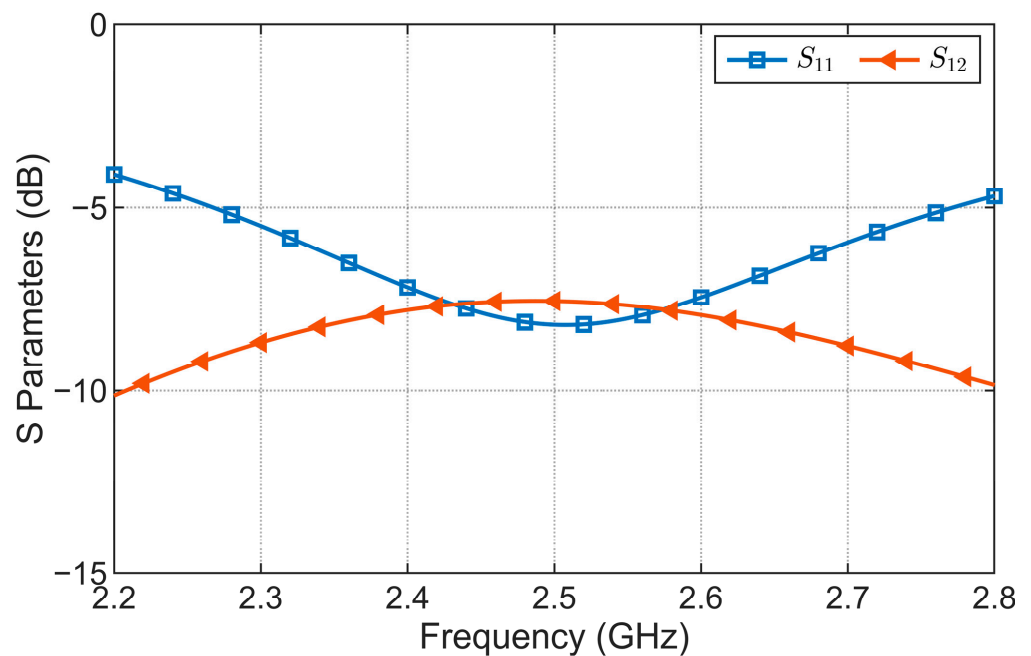


Figure 6. Simulated S parameters of the coupled array.

3.2. Realization of the Decoupling and Matching Network

The DMN of the three-element array is shown in Figure 7, which is obtained by substituting the ITS in Figure 3 and the NS in Figure 4 into the DMN in Figure 1; that is, TL1 and TL2 act as the ITS, while TL3 and TL4 act as the NS.

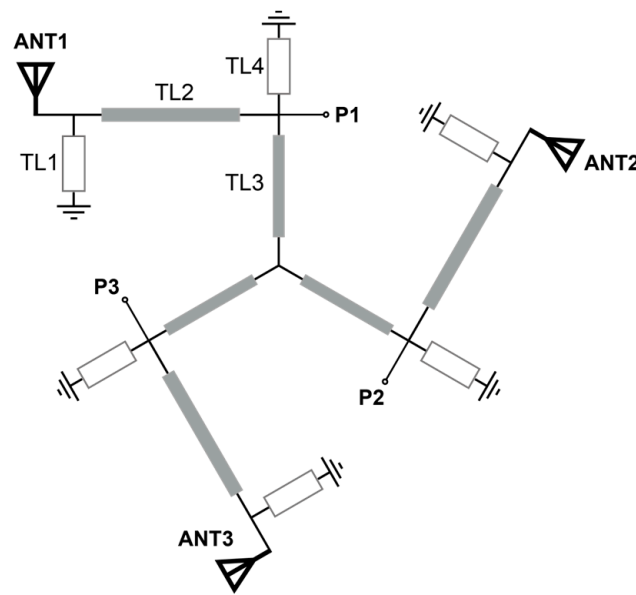


Figure 7. Diagram of the array cascaded with the DMN.

The admittance matrix at the reference plane t_1 are calculated as follows:

$$\mathbf{Y}^{t_1} = \begin{bmatrix} 29.38e^{-j67.1^\circ} & 16.19e^{j96.4^\circ} & 16.19e^{j96.4^\circ} \\ 16.19e^{j96.4^\circ} & 29.38e^{-j67.1^\circ} & 16.19e^{j96.4^\circ} \\ 16.19e^{j96.4^\circ} & 16.19e^{j96.4^\circ} & 29.38e^{-j67.1^\circ} \end{bmatrix} \text{ mS} \quad (13)$$

The odd and even mode admittances at the reference plane t_1 can be calculated by substituting the entries of the admittance matrix into Equation (4):

$$\begin{aligned} Y_e^{t_1} &= 9.629e^{j31.6^\circ} \text{ mS} \\ Y_o^{t_1} &= 45.09e^{-j73^\circ} \text{ mS} \end{aligned} \quad (14)$$

By setting the characteristic impedance of TL2 to 100 ohms, that is, $Y_2 = 0.01 \text{ S}$, and substituting the odd and even mode admittances into Equation (7), one can derive TL2's electrical length as follows:

$$\theta_2 = 2.21^\circ, 15.82^\circ \quad (15)$$

As the first value is too small, it is easily affected by discontinuities in the circuit and manufacturing errors; therefore, the second value 15.82° should be used. By substituting the two parameters of TL2 into Equation (8), the susceptance can be solved as $B_1 = 53.25 \text{ mS}$. As the susceptance value is greater than zero, an open-circuit transmission line stub is selected to realize it. A characteristic admittance of $Y_1 = 0.01 \text{ S}$ is determined for TL1, so an electrical length of 79.4° is obtained.

When the distance between adjacent transmission lines is greater than three times the line width, the coupling is low. It is therefore easier to bend the transmission line so as to achieve the miniaturization of the circuit with a smaller line width. It is important to note that, if the line width of the transmission line is too small, the electromagnetic simulation calculation amount will be too large, and the relative error of processing will increase if the line width is too small. Therefore, we selected transmission lines TL1 and TL2 with the same characteristic impedance of 100 ohms and a line width of 0.61 mm.

According to Figure 8, the impedance transformation section converts both the real part of the odd and even mode admittances into $Y_0 = 0.02 \text{ S}$ at the t_2 reference plane, with:

$$\begin{aligned} B_e^{t_2} &= -89.15 \text{ mS} \\ B_o^{t_2} &= 5.45 \text{ mS} \end{aligned} \quad (16)$$

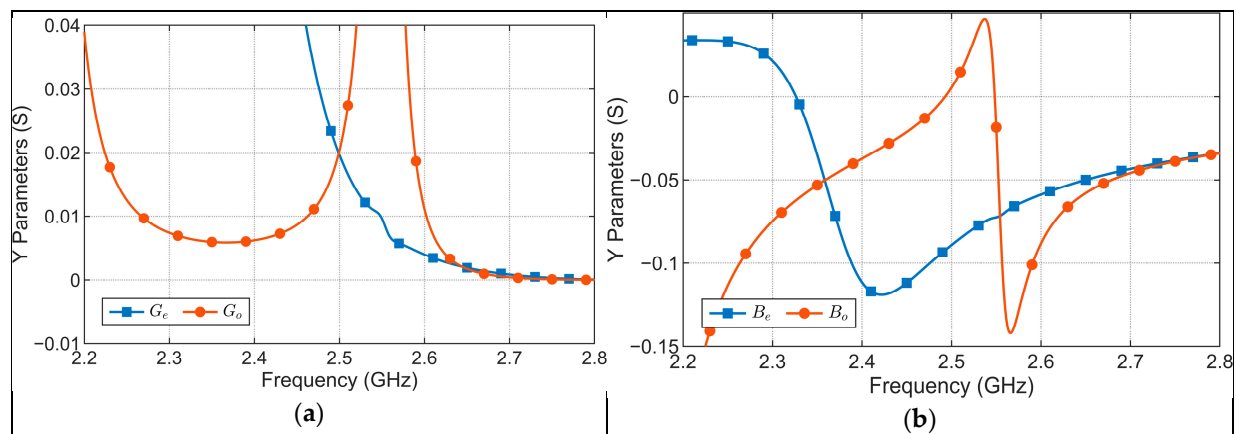


Figure 8. Y parameters at the reference plane t_2 : (a) real part of the even and odd admittances; and (b) imaginary part of the even and odd admittances.

By setting the characteristic impedance of TL3 to 100 ohms, that is, $Y_3 = 0.01$ S, and substituting the odd and even mode susceptances into Equation (11), one can derive TL3's electrical length as follows:

$$\theta_2 = 6.1^\circ, 83.9^\circ \quad (17)$$

For the first solution of the electrical length of TL3, it is impossible to form a star-shaped neutralization circuit because the sum of the lengths of TL2 and TL3 is less than the distance from the antenna installation position to the ground center, according to Figure 7. As a result, this solution must be discarded, and the electrical length of TL3 is 83.9° . By substituting the two parameters of TL3 into Equation (12), the susceptance can be solved as $B_4 = -4.38$ mS. As the susceptance value is less than zero, a short-circuit transmission line stub is selected to realize it. A characteristic admittance of $Y_4 = 0.01$ S is determined for TL1, so an electrical length of 66.3° is obtained.

Compared with Figure 8, the conductances of the odd and even modes remain the same, and the susceptances are zero at the operating frequency point, as shown in Figure 9. At the operating frequency point at reference plane t_3 , the odd and even mode admittances are Y_0 , thereby meeting the decoupling and matching condition and achieving the circuit function determined in the specification. As illustrated in Figure 10a, the surface current distribution of the DMN at 2.5 GHz can be verified. When one port feeds power, there is no energy coupling to the other two ports. Table 1 presents the parameters and dimensions of each segment of the transmission line of the DMN shown in Figure 10b.

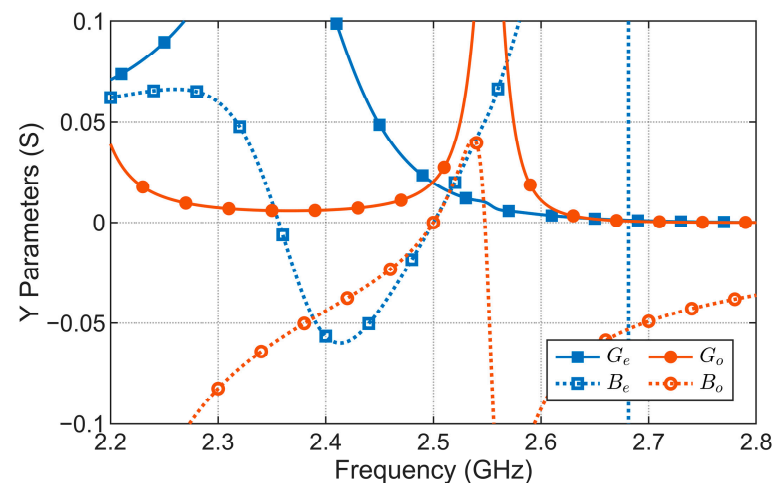


Figure 9. The even and odd admittances at reference plane t_3 .

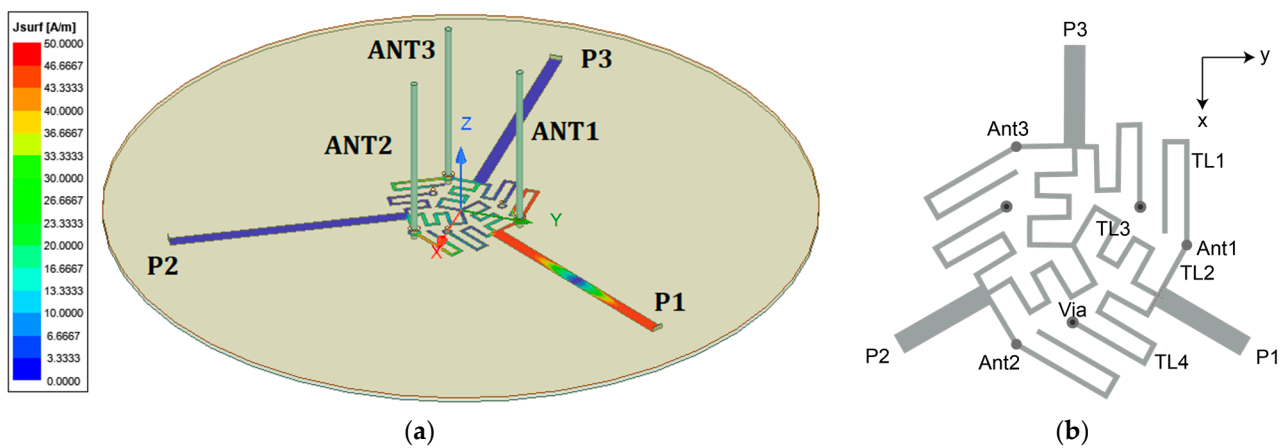


Figure 10. (a) The simulated current distribution on the DMN at the center frequency; and (b) the layout of the DMN.

Table 1. Design parameters of the DMN.

TL	Z (Ohm)	Θ (deg)	Width (mm)	Length (mm)
1	100	79.1	0.61	$9.5 + 2 + 8.5 = 20$
2	100	15.9	0.61	5.34
3	100	83.9	0.61	$2.5 + 3.5 + 2 + 3 + 2 + 3.69 + 2.5 + 4 = 22.9$
4	100	66.3	0.61	$2 + 4 + 2 + 6 + 2 + 7.5 = 23.5$

4. Measurements and Discussion

The decoupled antenna array prototype has been fabricated and tested in order to verify the effectiveness of the method proposed in this paper, as shown in Figure 11.

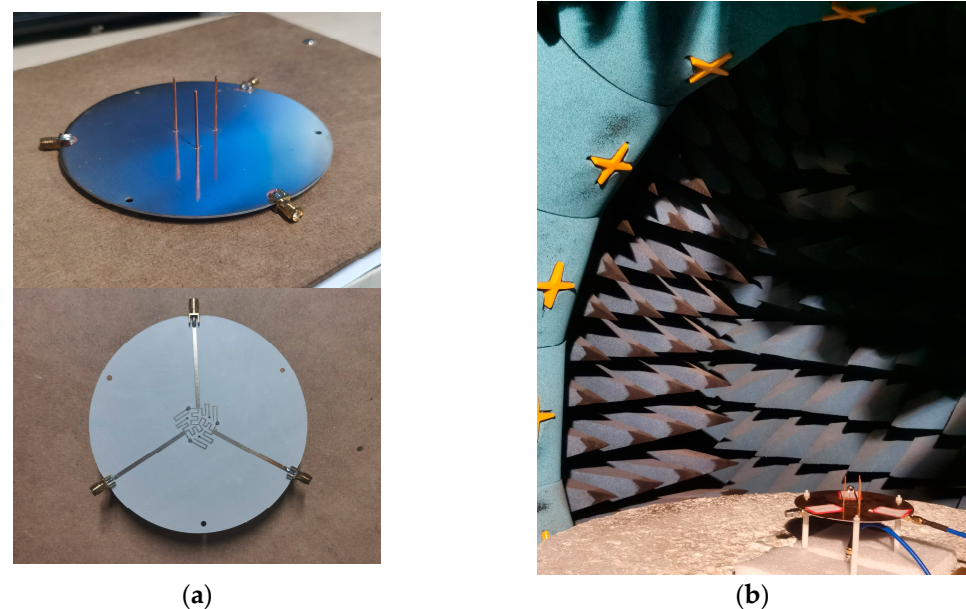


Figure 11. (a) Fabricated prototype; and (b) measurement in chamber.

As illustrated in Figure 11, a prototype decoupled antenna array has been constructed and tested for the verification of the effectiveness of the method proposed. The S parameters are shown in Figure 12. In comparison to these of the original design depicted in Figure 6, the measured return loss increases from 8.2 dB to 31.5 dB, and the measured port isolation increases from 7.6 dB to 33.5 dB. Comparing the simulation and test results of the

decoupling antenna array, the measured working frequency has been shifted by 14 MHz to the high-frequency direction, which may be primarily caused by a shorter antenna length than expected.

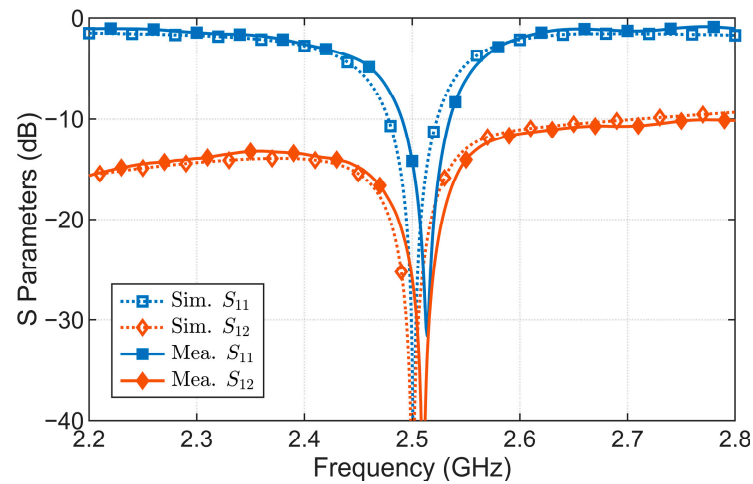


Figure 12. The S parameters of the decoupled array.

The maximum measured return loss of the array occurs at 2.514 GHz. The measured pattern of the decoupled array at 2.51 GHz is therefore compared with the simulated pattern at 2.5 GHz in Figure 13, when port 1 is excited. Figure 10a provides information on the position and orientation of the antenna in the co-ordinate system. According to (c), its maximum radiation direction lies along the $-y$ axis ($\varphi = 270^\circ$) when viewed in the xoy plane. The measured maximum gain of the antenna is 4.86 dBi at $\theta = 60^\circ$ as shown in (b). The antenna array radiates at 150° and 30° when ports 2 and 3 are activated, respectively, since the array is symmetrical. The simulated patterns in the xoz and yoz plane are symmetric, but the measured ones are not as symmetrical as the simulation results. The comparison of the simulated and measured patterns also indicates that the measured pattern has a higher cross-polarization level. They are both the result of manufacturing and assembly errors. There is difficulty in ensuring that the three antennas are installed with consistent lengths and are perpendicular to the ground. This results in a more current component that increases cross-polarization. The measured cross-polarization level is higher than the simulated value due to the angle between the antenna and the ground. As the angle deviates from 90° , the level of cross-polarization increases.

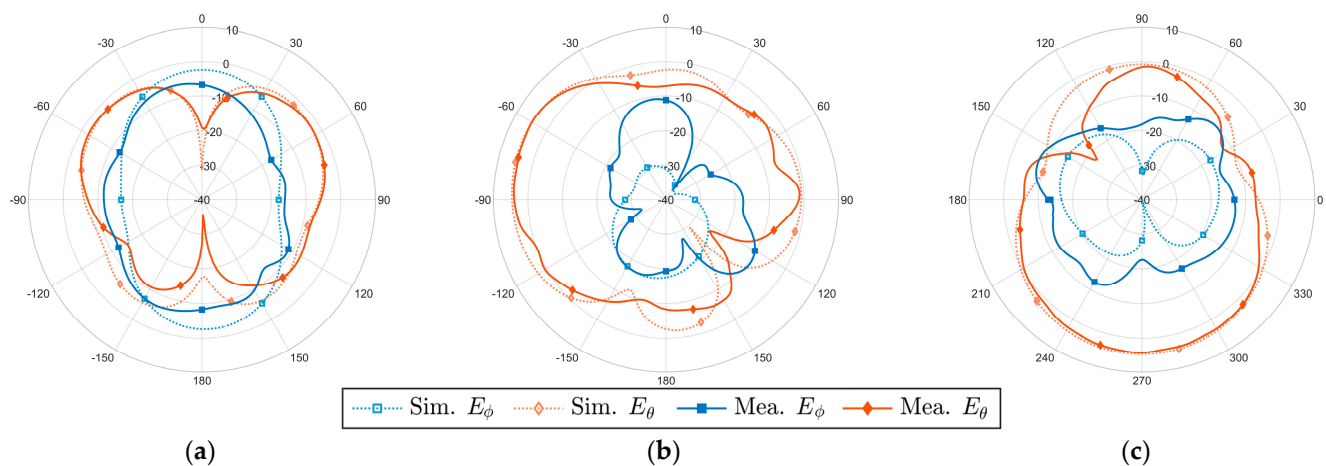


Figure 13. Radiation patterns of the decoupled array when port 1 is activated: (a) xoz plane; (b) yoz plane; and (c) xoy plane.

The radiation efficiency of the antenna is illustrated in Figure 14. According to the measured return loss maximum point, the measured frequency points are shifted to the right by 10 MHz compared with the simulated data. The measured antenna efficiency is greater than 72% near the center frequency point, whereas the simulated antenna efficiency is greater than 93%. Because the cable for measurement is not included in the simulation, there may be a discrepancy between the simulated and measured efficiency of the decoupled array. The measured efficiency of a monopole antenna operating at 2.5 GHz with a simulated efficiency of more than 95% in the measurement system is 85%. Considering the error of this measurement system, the difference between the simulation and measured data is within an acceptable range.

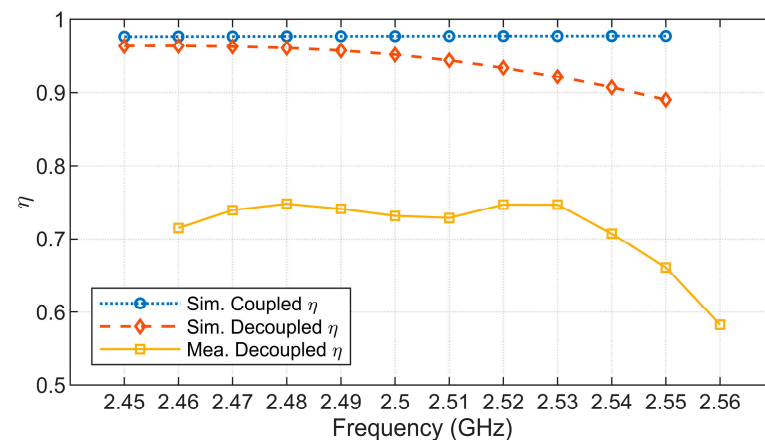


Figure 14. Antenna efficiency.

The envelope correlation coefficient (ECC) represents the correlation between antenna patterns, and its formula is as follows:

$$\rho_{ij} = \frac{\int |\bar{E}_i(\theta, \phi) \cdot \bar{E}_j^*(\theta, \phi)|^2 d\Omega}{\int |\bar{E}_i(\theta, \phi)|^2 d\Omega \cdot \int |\bar{E}_j(\theta, \phi)|^2 d\Omega} \quad (18)$$

As shown in Figure 15, the DMN reduces the ECC of the array from 0.105 to 0.0108 at the operating frequency.

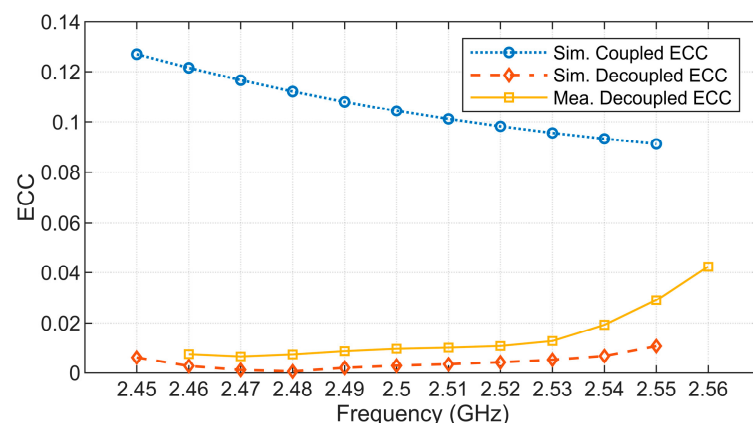


Figure 15. Envelope correlation coefficient.

The apparent diversity gain (ADG) measures the reliability of the communication links. By using the ECC calculated from the field pattern, it can be determined as

$$\text{ADG} = \sqrt{1 - \rho_{ij}^2} \quad (19)$$

It can be seen in Figure 15 that there are 11 frequency points with the ECC calculated from the field pattern, and their corresponding ADGs are all greater than 9.9 dB.

The decoupling circuit for the antenna array with three elements by using the eigen-mode method [32,33] is very complicated, in which at least two couplers are required, so it is not included in the comparison. Table 2 gives previous works on using the conjugate matching method [34–37] to decouple three-element antenna arrays. According to [34–37], the simulated scattering parameters of the coupled array and the measured scattering parameters of the decoupled array provide the port isolation value at the center frequency point, and the difference between these two values indicates that decoupling networks enhance the isolation at the center frequency point. Several of the decoupling circuit dimensions are given directly in [34–37], while others are derived from the antenna spacing and schematic diagrams. Compared with [37], which has the best performance in miniaturization, the solution presented in this paper has a relative size reduction of 17%. The proposed DMN not only obtains the optimal decoupling effect, but also minimizes the area of the decoupling and matching circuit.

Table 2. Comparison of decoupling techniques for three-element array.

#	Diameter of the Area Occupied by the Array	Diameter of the Area Occupied by the Network	Ratio of the Diameters	Isolation (dB)		
				Coupled	Decoupled	Enhancement
[34]	0.115 λ	1.27 λ	11.04	7.5	14.5	7
[35]	0.173 λ	0.61 λ	3.52	10.2	14.4	4.2
[36]	0.18 λ	0.79 λ	4.39	7.2	26	18.8
[37]	0.24 λ	0.41 λ	1.71	12	25	13
Proposed	0.173 λ	0.247 λ	1.42	7.6	33.5	25.9

5. Conclusions

This paper proposes a compact TL DMN for circular arrays with three elements. The compact DMN consists of an impedance transformation section and a star-shaped neutralization section. The impedance transformation section converts the odd and even mode conductances to the admittance of the system, and the neutralization circuits cancels the odd and even mode susceptances. The star-shaped circuit utilizes the area surrounded by the antennas in a more efficient manner than traditional triangle circuits. This facilitates the folding of the TL and the miniaturization of the circuit. Each module of the circuit is given a design formula after it has been analyzed analytically. A decoupling example is simulated and manufactured with the diameter of the area occupied by the DMN less than 0.247 λ . The port isolation is increased from 7.6 dB to 33.5 dB at the working frequency. The ECC between ports is reduced from 0.11 to 0.011, which validates the proposed method.

Author Contributions: Conceptualization, C.Z. and Y.-C.J.; data curation, C.Z.; formal analysis, C.Z.; investigation, C.Z.; methodology, C.Z. and Y.-C.J.; resources, C.Z.; software, C.Z.; supervision, Y.-C.J.; validation, C.Z.; visualization, C.Z.; writing—original draft, C.Z.; writing—review and editing, C.Z. and Y.-C.J. All authors have read and agreed to the published version of the manuscript.

Funding: This research received no external funding.

Institutional Review Board Statement: Not applicable.

Conflicts of Interest: The authors declare no conflict of interest.

References

- Robert, W., Jr. Heath, and Angel Lozano. In *Foundations of MIMO Communication*; Cambridge University Press: New York, NY, USA, 2019.
- Wallace, J.W.; Jensen, M.A.; Swindlehurst, A.L.; Jeffs, B.D. Experimental Characterization of the MIMO Wireless Channel: Data Acquisition and Analysis. *IEEE Trans. Wirel. Commun.* **2003**, *2*, 335–343. [CrossRef]

3. Vaughan, R.G.; Andersen, J.B. Antenna Diversity in Mobile Communications. *IEEE Trans. Veh. Technol.* **1987**, *36*, 149–172. [\[CrossRef\]](#)
4. BharathiDevi, B.; Kumar, J. Small Frequency Range Discrete Bandwidth Tunable Multiband MIMO Antenna for Radio/Lte/Ism-2.4 ghz Band Applications. *AEU—Int. J. Electron. Commun.* **2022**, *144*, 154060. [\[CrossRef\]](#)
5. Ding, C.F.; Zhang, X.Y.; Xue, C.D. Novel Pattern-Diversity-Based Decoupling Method and Its Application to Multielement MIMO Antenna. *IEEE Trans. Antennas Propag.* **2018**, *66*, 4976–4985. [\[CrossRef\]](#)
6. Kumar, P.; Urooj, S.; Malibari, A. Design of Quad-Port Ultra-Wideband Multiple-Input-Multiple-Output Antenna with Wide Axial-Ratio Bandwidth. *Sensors* **2020**, *20*, 1174. [\[CrossRef\]](#)
7. Kollipara, V.; Peddakrishna, S. Quad-Port Circularly Polarized MIMO Antenna with Wide Axial Ratio. *Sensors* **2022**, *22*, 7972. [\[CrossRef\]](#)
8. Yan, S.; Zheng, Y.; Wang, B.; Zhang, J.; Vandenbosch, G.A. A Miniaturized Extremely Close-Spaced Four-Element Dual-Band MIMO Antenna System with Polarization and Pattern Diversity. *IEEE Antennas Wirel. Propag. Lett.* **2018**, *17*, 134–137.
9. Wu, T.Y.; Fang, S.T.; Wong, K.L. Printed Diversity Monopole Antenna for Wlan Operation. *Electron. Lett.* **2002**, *38*, 1625–1626. [\[CrossRef\]](#)
10. Hwang, J.N.; Chung, S.J. Isolation Enhancement between Two Packed Antennas with Coupling Element. *IEEE Antennas Wirel. Propag. Lett.* **2011**, *10*, 1263–1266. [\[CrossRef\]](#)
11. Yao, Y.; Wang, X.; Chen, X.; Yu, J.; Liu, S. Novel Diversity/MIMO Pifa Antenna with Broadband Circular Polarization for Multimode Satellite Navigation. *IEEE Antennas Wirel. Propag. Lett.* **2012**, *11*, 65–68.
12. Abedin, M.F.; Ali, M. Effects of a Smaller Unit Cell Planar Ebg Structure on the Mutual Coupling of a Printed Dipole Array. *IEEE Antennas Wirel. Propag. Lett.* **2005**, *4*, 274–276. [\[CrossRef\]](#)
13. Payandehjoo, K.; Abhari, R. Employing Ebg Structures in Multiantenna Systems for Improving Isolation and Diversity Gain. *IEEE Antennas Wirel. Propag. Lett.* **2009**, *8*, 1162–1165. [\[CrossRef\]](#)
14. Mavridou, M.; Feresidis, A.P.; Gardner, P. Tunable Double-Layer Ebg Structures and Application to Antenna Isolation. *IEEE Trans. Antennas Propag.* **2016**, *64*, 70–79. [\[CrossRef\]](#)
15. Kumar, J. Compact MIMO Antenna. *Microw. Opt. Technol. Lett.* **2016**, *58*, 1294–1298. [\[CrossRef\]](#)
16. Park, J.; Choi, J.; Park, J.Y.; Kim, Y.S. Study of a T-Shaped Slot with a Capacitor for High Isolation between MIMO Antennas. *IEEE Antennas Wirel. Propag. Lett.* **2012**, *11*, 1541–1544. [\[CrossRef\]](#)
17. Chiu, C.Y.; Cheng, C.H.; Murch, R.D.; Rowell, C.R. Reduction of Mutual Coupling between Closely-Packed Antenna Elements. *IEEE Trans. Antennas Propag.* **2007**, *55*, 1732–1738. [\[CrossRef\]](#)
18. Karaboikis, M.; Soras, C.; Tsachtsiris, G.; Makios, V. Compact Dual-Printed Inverted-F Antenna Diversity Systems for Portable Wireless Devices. *IEEE Antennas Wirel. Propag. Lett.* **2004**, *3*, 9–14. [\[CrossRef\]](#)
19. Ahn, D.; Park, J.S.; Kim, C.S.; Kim, J.; Qian, Y.; Itoh, T. A Design of the Low-Pass Filter Using the Novel Microstrip Defected Ground Structure. *IEEE Trans. Microw. Theory Tech.* **2001**, *49*, 86–93. [\[CrossRef\]](#)
20. Diallo, A.; Luxey, C.; Le Thuc, P.; Staraj, R.; Kossiavas, G. Study and Reduction of the Mutual Coupling between Two Mobile Phone Pifas Operating in the Dcs1800 and Umts Bands. *IEEE Trans. Antennas Propag.* **2006**, *54*, 3063–3074. [\[CrossRef\]](#)
21. Su, S.W.; Lee, C.T.; Chang, F.S. Printed MIMO-Antenna System Using Neutralization-Line Technique for Wireless Usb-Dongle Applications. *IEEE Trans. Antennas Propag.* **2012**, *60*, 456–463. [\[CrossRef\]](#)
22. Su, S.W.; Lee, C.T.; Chen, S.C. Very-Low-Profile, Triband, Two-Antenna System for Wlan Notebook Computers. *IEEE Antennas Wirel. Propag. Lett.* **2018**, *17*, 1626–1629. [\[CrossRef\]](#)
23. Deng, C.; Liu, D.; Lv, X. Tightly-Arranged Four-Element MIMO Antennas for 5g Mobile Terminals. *IEEE Trans. Antennas Propag.* **2019**, *67*, 6353–6361. [\[CrossRef\]](#)
24. Mak, A.C.; Rowell, C.R.; Murch, R.D. Isolation Enhancement between Two Closely Packed Antennas. *IEEE Trans. Antennas Propag.* **2008**, *56*, 3411–3419. [\[CrossRef\]](#)
25. Lau, B.K.; Andersen, J.B. Simple and Efficient Decoupling of Compact Arrays with Parasitic Scatterers. *IEEE Trans. Antennas Propag.* **2012**, *60*, 464–472. [\[CrossRef\]](#)
26. Zhang, S.; Lau, B.K.; Tan, Y.; Ying, Z.; He, S. Mutual Coupling Reduction of Two Pifas with a T-Shape Slot Impedance Transformer for MIMO Mobile Terminals. *IEEE Trans. Antennas Propag.* **2012**, *60*, 1521–1531. [\[CrossRef\]](#)
27. Zhai, G.; Chen, Z.N.; Qing, X. Mutual Coupling Reduction of a Closely Spaced Four-Element MIMO Antenna System Using Discrete Mushrooms. *IEEE Trans. Microw. Theory Tech.* **2016**, *64*, 3060–3067. [\[CrossRef\]](#)
28. Dhevi, B.L.; Vishvakshnan, K.S.; Rajakani, K. Isolation Enhancement in Dual-Band Microstrip Antenna Array Using Asymmetric Loop Resonator. *IEEE Antennas Wirel. Propag. Lett.* **2018**, *17*, 238–241. [\[CrossRef\]](#)
29. Roshani, S.; Shahveisi, H. Mutual Coupling Reduction in Microstrip Patch Antenna Arrays Using Simple Microstrip Resonator. *Wirel. Pers. Commun.* **2022**, *126*, 1665–1677. [\[CrossRef\]](#)
30. Kedze, K.E.; Zhou, W.; Labossiere, J.; Javanbakht, N.; Shaker, J.; Amaya, R.E. Suppression of Mutual Coupling in Dual Differentially Fed Microstrip Patch Array Antenna. In Proceedings of the 2022 IEEE International Symposium on Antennas and Propagation and USNC-URSI Radio Science Meeting (AP-S/URSI), Denver, CO, USA, 10–15 July 2022.
31. Javanbakht, N.; Ahmed, I.; Cooper, M.; Jarosz, M. Impedance Bandwidth and Gain Improvement of Patch Array Antenna. In Proceedings of the 2022 IEEE International Symposium on Phased Array Systems & Technology (PAST), Waltham, MA, USA, 11–14 October 2022.

32. Volmer, C.; Weber, J.; Stephan, R.; Blau, K.; Hein, M.A. An Eigen-Analysis of Compact Antenna Arrays and Its Application to Port Decoupling. *IEEE Trans. Antennas Propag.* **2008**, *56*, 360–370. [[CrossRef](#)]
33. Yeung, L.K. A Mode-Based Technique for Compact Linear MIMO Arrays. In Proceedings of the 2011 IEEE MTT-S International Microwave Symposium, Baltimore, MD, USA, 5–10 June 2011.
34. Chua, P.T.; Coetzee, J.C. Microstrip Decoupling Networks for Low-Order Multiport Arrays with Reduced Element Spacing. *Microw. Opt. Technol. Lett.* **2005**, *46*, 592–597. [[CrossRef](#)]
35. Sheel, S.; Albannay, M.M.; Coetzee, J.C. Integrated Decoupling and Matching Network Incorporated in the Ground Plane of a Compact Monopole Array. *Microw. Opt. Technol. Lett.* **2015**, *57*, 1315–1319. [[CrossRef](#)]
36. Li, M.; Jiang, L.; Yeung, K.L. Novel and Efficient Parasitic Decoupling Network for Closely Coupled Antennas. *IEEE Trans. Antennas Propag.* **2019**, *67*, 3574–3585. [[CrossRef](#)]
37. Zhao, L.; Wu, K.L. A Broadband Coupled Resonator Decoupling Network for a Three-Element Compact Array. In Proceedings of the 2013 IEEE MTT-S International Microwave Symposium Digest (MTT), Seattle, WA, USA, 2–7 June 2013.
38. Reed, J.; Wheeler, G.J. A Method of Analysis of Symmetrical Four-Port Networks. *IRE Trans. Microw. Theory Tech.* **1956**, *4*, 246–252. [[CrossRef](#)]
39. Roshani, S.; Yahya, S.I.; Rastad, J.; Mezaal, Y.S.; Liu, L.W.; Roshani, S. Design of a Filtering Power Divider with Simple Symmetric Structure Using Stubs. *Symmetry* **2022**, *14*, 1973. [[CrossRef](#)]
40. Wu, C.H.; Zhou, G.T.; Wu, Y.L.; Ma, T.G. Stub-Loaded Reactive Decoupling Network for Two-Element Array Using Even–Odd Analysis. *IEEE Antennas Wirel. Propag. Lett.* **2013**, *12*, 452–455. [[CrossRef](#)]

Disclaimer/Publisher’s Note: The statements, opinions and data contained in all publications are solely those of the individual author(s) and contributor(s) and not of MDPI and/or the editor(s). MDPI and/or the editor(s) disclaim responsibility for any injury to people or property resulting from any ideas, methods, instructions or products referred to in the content.